

Efficient Polysulfides Conversion Kinetics Enabled by Ni@CNF Interlayer for Lithium Sulfur Batteries

I. Rakhimbek¹, N. Baikalov², A. Konarov², A. Mentbayeva², Y. Zhang³,
Z. Mansurov⁴, M. Wakihara⁵, Zh. Bakenov^{1,2*}

¹National Laboratory Astana, Nazarbayev University, 53, Kabanbay batyr ave., Astana, Kazakhstan

²Department of Chemical and Materials Engineering, Nazarbayev University,
53, Kabanbay batyr Ave., Astana, Kazakhstan

³Dalian Institute of Chemical Physics, Chinese Academy of Sciences,
No. 457 Zhongshan Road, Dalian, Liaoning, 116023, China

⁴Institute of Combustion Problems, 172 Bogenbay Batyr str., Almaty, Kazakhstan

⁵Tokyo Institute of Technology, T2 Chome-12-1 Ookayama, Meguro City, Tokyo 152-8550, Japan

Article info

Received:
24 April 2023

Received in revised form:
27 May 2023

Accepted:
2 July 2023

Abstract

Recent advances in the development of lithium-sulfur batteries (Li-S) demonstrated their high effectiveness owing to their tremendous theoretical specific capacity and high theoretical gravimetric energy. Nevertheless, the potential commercialization of Li-S is significantly held by the insulating nature of sulfur and complicated RedOx reactions during the electrochemical charge-discharge processes. This paper presents nickel nanoparticles embedded carbon nanofibers interlayer (Ni@CNF) between a cathode and a separator as an additional physical barrier against lithium polysulfides shuttle for their efficient conversion during the charge-discharge cycling. Furthermore, the interlayer provides an auxiliary electron pathway with subsequent lowering of the charge transfer resistance. The electrochemical analysis of a Li-S cell with the Ni@CNF interlayer demonstrated high initial discharge capacities of 1441.2 mAh g⁻¹ and 1194.2 mAh g⁻¹ at 0.1 and 1.0 C rates, respectively, with remarkable capacity retention of ~83% after 100 cycles. This study revealed the advantageous impact of Ni@CNF towards solving the major issues of lithium-sulfur batteries, i.e., sluggish kinetics and the shuttle effect.

1. Introduction

The rapid development of portable electronics and electric transportation technologies requires next-generation energy storage systems capable of providing sufficient generated power and energy. However, currently employed lithium-ion batteries keep struggling to meet the rapidly escalating demand for long-life and high-energy density energy storage systems [1, 2]. Thus, the development of an alternative approach regarding the fulfillment of the mentioned issues along with utilizing cost-effective

and environmentally friendly materials is of utmost importance. The recent advances in the development of lithium-sulfur batteries (Li-S) have demonstrated exciting perspectives of these systems coming from their attractive performance parameters: the theoretical specific capacity of 1675 mAh g⁻¹ and theoretical energy density of 2567 Wh kg⁻¹, which are several times greater than that of conventional lithium-ion batteries. In addition to that, the sulfur cathode has other advantages such as low cost, widespread abundance, and environmental friendliness [3–5].

Nevertheless, the desired development and commercialization of Li-S is considerably hindered by several crucial challenges. To begin with, the insulating

*Corresponding author.

E-mail address: Zbakenov@nu.edu.kz

nature of sulfur and discharge products, $\text{Li}_2\text{S}/\text{Li}_2\text{S}_2$, lead to poor sulfur utilization during charge/discharge processes [6]. Secondly, the lithiation to lithium sulfides results in the large volumetric expansion of sulfur (~80%) and may end up pulverizing and crushing the electrode [7]. Lastly, among the major issues, a significant capacity loss occurs with the formation of intermediate long-chain lithium polysulfides (LiPS), their dissolution in the electrolyte, and diffusion to the lithium anode side of the cell bypassing the separator, thus physically shuttling and limiting the ion exchange [8, 9]. The described phenomenon is also known as the 'shuttle effect'.

Nowadays the most common approach to address these issues is to encapsulate sulfur in a matrix of conductive materials with microporous structures like carbon-based hosts (carbon nanofibers, carbon nanotubes, graphene, and/or their hybrids) [10, 11]. The reason behind relying on carbon materials is owing to their high conductivity and ability to act as physical barriers for polysulfide shuttle. As a result, a noticeable improvement in sulfur utilization towards to practical applications of Li-S cells has been achieved [12, 13]. Nevertheless, although carbon remains the most suitable host for sulfur, its nonpolar planes have substantial limitations with chemically anchoring of polar LiPS molecules [14, 15].

In this regard, the implementation of nanostructured polar inorganic compounds (transition metal nanoparticles [16]; metal oxides [17], sulfides, and nitrides [18]; etc.) was widely presented as a way to enhance the chemical affinity of carbon hosts towards LiPS. The beneficial impact of such materials was on the stronger LiPS adsorption, and subsequent rendering of Li-S cells with higher sulfur utilization. Among them, the metal catalysts – ferrolites and noble metals – demonstrated a great increase in LiPS interaction with the carbonaceous matrix leading to the enhanced kinetics of RedOx reactions and a remarkably improved overall conductivity [9, 19]. However, the toxicity concerns (the use of toxic cobalt) and the high cost of noble metals (platinum, palladium) limit their efficient usage in energy storage systems. That is why, a more universal metal catalyst, which is able to address the problems of Li-S and is a cost-effective material is required for the realization of this approach. Nickel (Ni) has attracted considerable attention justified by its remarkable catalytic features comparable to that of noble metals but being significantly cheaper, demonstrating excellent chemical affinity towards LiPS and having considerably lower hazardous effects on the surrounding environment than cobalt [9, 20, 21].

Apart from the materials implemented in Li-S, the cell's configuration plays a huge role, too, especially when it comes to more uniform utilization of the active material. Recent developments in lithium-sulfur batteries suggested including a carbon-based interlayer membrane (carbon nanofibers [22], multi-walled carbon nanotubes [23], graphene [24], etc.) between cathode and separator that would be applied not only as a physical barrier against LiPS but also providing additional charge transfer pathways [25–27]. However, it has the same disadvantages as a bare carbon matrix host for sulfur. That is why, recently presented novel interlayer films in most cases include embedded inorganic metal compounds for enhanced electrochemical performance Li-S batteries [26, 28]. Consequently, an interlayer membrane with nickel nanoparticles was introduced, which can efficiently mitigate the LiPS diffusion by physical blocking and chemical binding, thus, greatly enhancing the reactions kinetics and overall cell performance.

In this paper, the interlayer membrane based on carbon nanofibers with nickel nanoparticles (Ni@CNF) was employed to improve the reactions kinetics of Li-S cells. The interlayer was fabricated by the electrospinning technique and subsequent heat treatment in a tubular furnace. The cathodic side consisted of a conventional matrix based on sulfur loaded into conductive Ketjen Black (KB) in a ratio of S:KB = 7:3. KB possesses a large surface area and a large pore volume sufficient to create a sulfur-carbon composite electrode (S@KB) and crucial to avoid the electrode crushing caused by the sulfur expansion. Analysis of the Ni@CNF interlayer impact on Li-S batteries demonstrated the enhanced RedOx reactions kinetics of charge/discharge processes, decreased charge transfer resistance owing to implementing additional electron pathways with polar Ni nanoparticles, and showed overall beneficial effects on charge-discharge cyclability of the cell.

2. Methodology

2.1 Fabrication of carbon nanofiber interlayers

The carbon nanofiber interlayer mats – both CNF and Ni@CNF – were initially fabricated by the electrospinning method followed by heat treatment in a tubular furnace. The synthesis of the Ni@CNF composite began with dissolving 1.25 g of $\text{Ni}(\text{Ac})_2$ in 20 mL of dimethylformamide (DMF) under vigorous mixing by a magnetic stirrer. When the solution turned into a non-transparent emerald homogeneous colour, 2.4 g of polyacrylonitrile (PAN) was

gradually added to avoid the formation of lumps and left stirred for 10 more hours. After that, the solution was transferred into a 20 mL syringe inside an electrospinning chamber (Inovenso Ne200, Turkey) and drawn out as long-thread polymeric nanofibers on an aluminum-covered rotating drum after being exposed to the electric field. The conditions of the electrospinning procedure were set as follows: the distance between the rotating drum and the nozzle connected to the syringe by the flexible tube was 17 cm; the rate of the solution pressing from the syringe was 2 mL h⁻¹; the applied voltage was 20 kV; the rate of the drum's rotation was 250 rpm; the overall coating time took up to 8 h. The subsequent heating of the collected nanofibers took place in the tube furnace (Across International STF 1200, USA) initially at 280 °C in the air for 2 h with a 5 °C min⁻¹ heating rate. This step allowed to enrich the nanofibers with oxygen, which initiates anchoring bridges between carbon formed and Ni nanoparticles for better durability and flexibility of the material. Next, an additional heat treatment was done at 700 °C in an argon atmosphere for 2 h with a heating rate of 2 °C min⁻¹, which allowed simultaneous carbonization of polymeric nanofibers and transformation of nickel acetate into Ni and NiO nanoparticles. Finally, the resulting carbon nanofiber mats were heated at 500 °C in an argon+hydrogen atmosphere for 3 h with a 5 °C min⁻¹ heating rate to reduce nickel oxide nanoparticles into pure nickel. The obtained material was a self-standing flexible film. Fabrication of a bare CNF without Ni nanoparticles followed the same procedures under the same set of parameters but required only PAN dissolution in DMF and the first two heat treatments out of three in the tubular furnace. To use in Li-S cells, the carbon nanofiber mats were cut into round-shaped discs (d = 19 mm) by an electrode disc cutter.

2.2 Materials characterization

The crystal structure of synthesized carbon nanofiber mats was analysed employing X-ray diffraction (Rigaku Smartlab) with Cu K α radiation ($\lambda = 1.54056$ Å) in the range of 10 to 90° 2 θ . The chemical structure of the samples and phase transitions were studied by Raman spectroscopy (Horiba LabRam Evolution) with x10 objective and 532 nm laser. The pore size distribution measurements were conducted by a nitrogen porosimetry (Nitrogen porosimeter, Quantachrome Instruments) by Batter-Joyner-Halenda (BJH) method, while the pore volume was identified by the adsorption and desorption isotherms. The

surface morphology and nanostructure of carbon nanofibers were characterized by scanning electron microscopy (SEM, Zeiss Crossbeam 540) and transmitting electron microscopy (TEM, Jeol JEM-1400 PLUS). The elements distribution in the samples was identified by energy-dispersive X-ray spectroscopy (EDS, Zeiss Crossbeam 540). The chemical binding status and valence changes were investigated using an X-ray photoelectron spectroscopy (NEXSA, Thermo Scientific) with correlations to C 1s spectra.

2.3 Sulfur cathode fabrication

The S@KB sulfur composite cathode for Li-S cells consisted of sulfur impregnated in Ketjen Black (S@KB). To begin with, sulfur and Ketjen Black were dried in a vacuum oven at 60 °C overnight. Then, the materials were thoroughly mixed in an agate mortar in a weight ratio of 7:3 (S:KB) reaching uniform grey coloring. Next, the powder mix was sealed in an autoclave inside the glovebox filled with argon and then heated in a muffle furnace. The resulting composite was used to prepare the electrode by mixing with acetylene black (AB, conductive agent) and polyvinylidene fluoride (PVDF, binding material) in a weight ratio of 8:1:1. Further, N-methyl pyrrolidone (NMP, solvent) was added to the mixture to obtain the cathode slurry, which was cast on carbon-coated aluminum foil by doctor blade technique. Hereafter, the electrode was dried in a vacuum oven at 60 °C overnight. The prepared electrode was cut into round-shaped discs (d = 16 mm) and was used to assemble Li-S cells.

2.4 Li-S cells assembling

Li-S cells with interlayer membranes were based on CR2032 coin-type cells and assembled in an MBRAUN LABMaster glovebox filled with argon (oxygen and moisture levels < 0.1 ppm). The cells consisted of the S@KB cathode, the Ni@CNF or CNF interlayer, Celgard 2400 separator, Li metal as both counter and reference electrode, and 1 M LiTFSI in 1,3-dioxolane (DOL)/1,2-dimethoxyethane (DME) (v/v, 1:1) electrolyte with 2 wt.% of LiNO₃. The fabrication of a cell was as follows: the cathode was placed inside a coin cell's positive cap and covered with the carbon nanofiber interlayer. Then, 25 μ L of the electrolyte was added dropwise and subsequently covered by the separator. After that, another 25 μ L of the electrolyte was added, and the Li metal chip was put on the top. Lastly, the cell was sealed and pressed by a crimping machine (Hohsen Inc., Japan).

2.5 Electrochemical performance

The impact of CNF and Ni@CNF interlayers on the electrochemical performance of Li-S batteries was investigated by a set of electrochemical methods. The RedOx processes and their polarization trends were investigated by cyclic voltammetry (CV) at a scan rate of 0.1 mV s^{-1} in a potential range from 1.6 to 2.8 V on a potentiostat/galvanostat VMP3 (Biologic Inc.). The charge transfer resistance tendencies during the RedOx reactions were studied by the electrochemical impedance spectroscopy (PEIS) performed on VMP3 within a frequency range from 100 kHz to 1 MHz. The reversibility and stability of electrochemical reactions were analyzed by the galvanostatic charge-discharge tests on a NewAre battery tester BTS-4000 at 0.1 and 1.0 C current densities with subsequent potential profile recordings.

2.6 Symmetric cells analysis

The study of the extent of lithium polysulfides conversion during RedOx reactions was carried out via assembling symmetric cells and analysing the CV profiles recorded at 0.5 mV s^{-1} scan rate in a potential range from -1.5 V to 1.5 V on VMP3 potentiostat/galvanostat. The cells included two identical electrodes made from the synthesized membranes (either with Ni@CNF or CNF) separated by a commercial Celgard 2400 membrane and with 50 μL of 0.05 M Li_2S_6 solution as a source of sulfur species and electrolyte.

stat/galvanostat. The cells included two identical electrodes made from the synthesized membranes (either with Ni@CNF or CNF) separated by a commercial Celgard 2400 membrane and with 50 μL of 0.05 M Li_2S_6 solution as a source of sulfur species and electrolyte.

3. Results and discussion

3.1 Materials characterization

Ni@CNF and CNF interlayer membranes were successfully synthesized according to the Methodology, Section 2.1.

The crystal structure of Ni@CNF and CNF are presented as X-ray diffraction patterns in Fig. 1a. Both materials had two peaks around $2\theta = 24^\circ$, 45° of graphitized carbon phase, which is the most significant contributor to the overall conductivity. Meanwhile, the recrystallization of Ni NPs was observed in the XRD pattern of Ni@CNF as reflections at $2\theta = 44^\circ$, 51° , and 76° corresponding to (111), (200), and (220) interplanar spacings of pure Ni. The relative content of the ordered/disordered structures of carbon was estimated by calculating and comparing the ratio of D and G band peaks at Raman spectra.

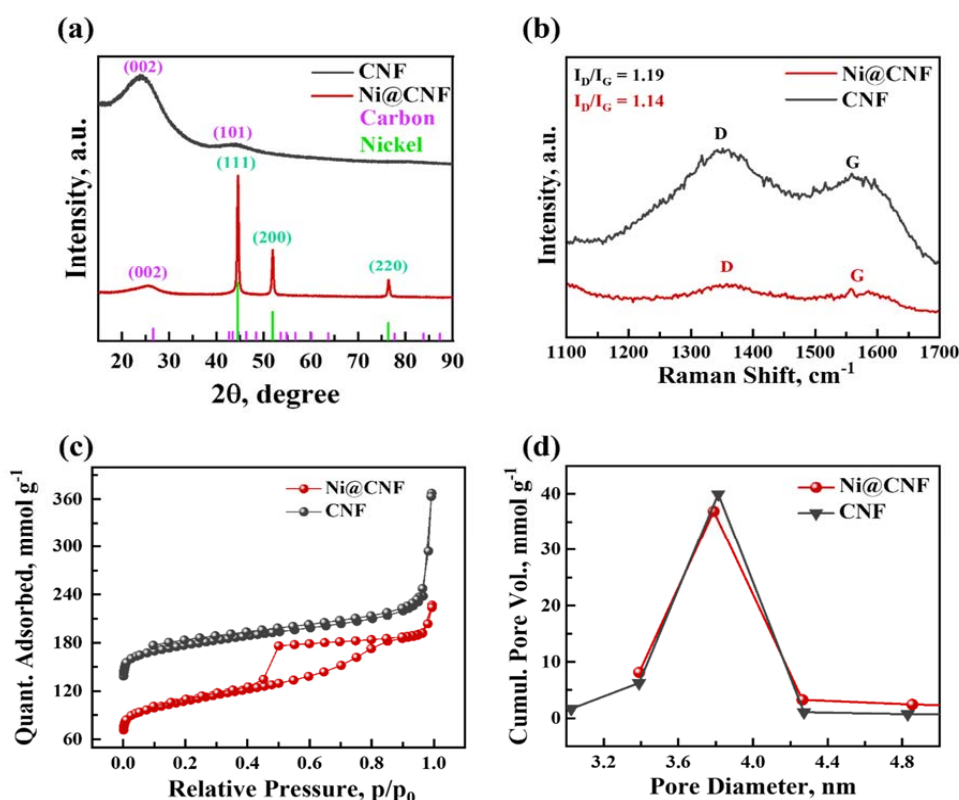


Fig. 1. Characterization of Ni@CNF and CNF: (a) – X-ray diffraction patterns; (b) – Raman spectrum; (c) – Adsorption-desorption isotherms; (d) – BJH pore-distribution analysis.

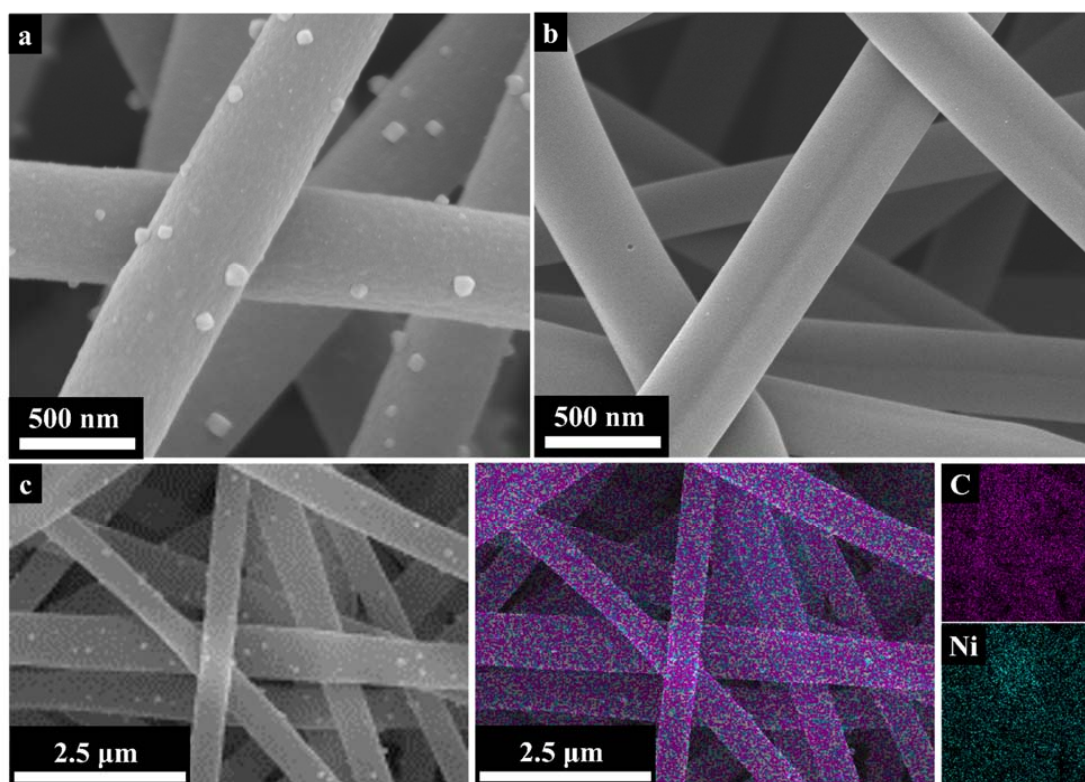


Fig. 2. Morphological analysis of carbon nanofiber mats. Scanning Electron Microscopy characterization of: (a) – Ni@CNF, (b) – CNF; (c) – EDS-mapping of Ni@CNF with C and Ni regions.

The D band had the higher intensity, which indicated the presence of more disordered amorphous carbon than the ordered one (Fig. 1b). The extent of the ratio shifting between the bands implied possible structure defects and shifts in the grain boundaries that could affect the agglomeration of nanoparticles [29, 30]. Nitrogen porosimetry was employed to investigate the materials' pore characteristics and, according to the BJH method, demonstrated that the average diameter of pores was approximately ~ 3.817 nm for both Ni@CNF and CNF (Fig. 1c). In addition, the extent of adsorbed nitrogen presented as adsorption-desorption isotherms pointed at higher adsorbed quantities by CNF, thus implying a higher specific surface area, rather than Ni@CNF, which could be the result of possible pores blocking by Ni NPs (Fig. 1d).

The surface morphology analysis performed by scanning electron microscopy (SEM) showed the formation of porous long carbon nanofibers with an average diameter of 400-500 nm (Fig. 2a) alongside uniform Ni NPs ($d \sim 20$ nm) recrystallized on the surface of the Ni@CNF composite (Fig. 2b). The extent of the Ni NPs distribution was additionally studied by the energy dispersive spectrometry (EDS) mapping of the C and Ni elements (Fig. 2c), which revealed the absence of the nanoparticles agglomeration. More-

over, the uniform structure indicated enhanced lithium polysulfides capturing by the carbon nanofibers and increased conversion by Ni NPs.

Further morphological analysis was carried out by high-resolution transmission electron microscopy as illustrated in Fig. 3. The TEM images of Ni@CNF (Fig. 3a) and CNF (Fig. 3b) demonstrate non-hollow structures of carbon nanofibers and the presence of Ni NPs not only on the surface but also inside the carbon nanofibers. This finding indicates that the formation of Ni NPs had a strong connection with the main carbon structure, presumably owing mostly to the oxygen bridges between Ni and C.

High-resolution X-ray photoelectron spectroscopy was employed to investigate the elemental binding status along with the surface chemistry of the synthesized carbon nanofiber mats. According to the findings, the survey spectra confirmed the presence of C, O, N, and Ni elements in Ni@CNF without noticeable impurities (Fig. 4a). The high-resolution C 1s spectra demonstrated deconvolution of the main signal into four sub-peaks arising at 284.78 eV, 285.88 eV, 286.78 eV, and 290.08 eV corresponding to C-C, C-N, C-O, and O=C-O functional groups, respectively (Fig. 4b). The formation of C-N suggests possible nitrogen doping of the carbon host delivered from the nitrogen group of polyacrylonitrile,

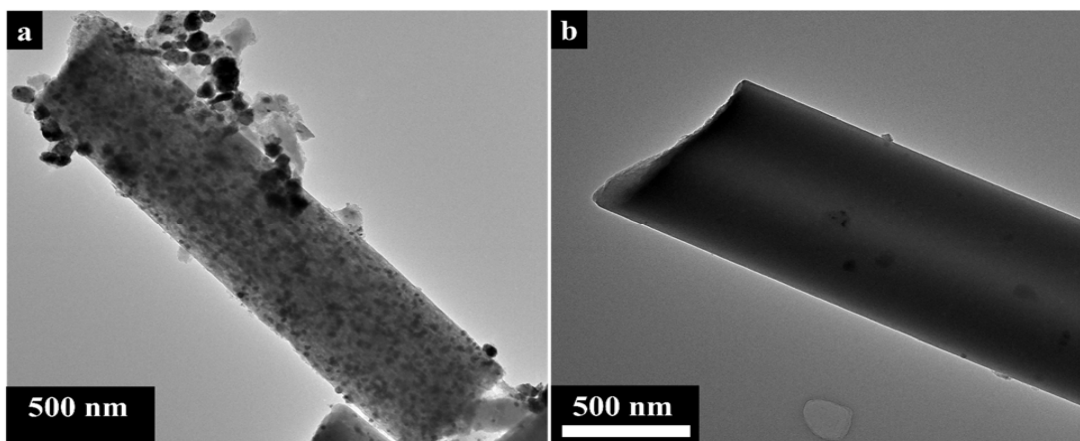


Fig. 3. Morphological analysis of carbon nanofiber mats by High-Resolution Transmission Electron Microscopy: (a) – Ni@CNF image; (b) – CNF image.

thus, increasing the material's conductivity, while C-O and O=C-O groups, most likely, arose due to the surface oxidation. The N 1s spectra were presented as four deconvoluted subpeaks of Pyridinic N, Graphitic N, Pyrrolic N, and oxidized N groups at 398.48 eV, 399.28 eV, 400.68 eV, and 404.58 eV, correspondingly (Fig. 4c). The presence of nitrogen groups was of much importance due to promoting enhanced conductivity as well as being used as a Lewis base supportive contributor to the polar LiPS adsorption by the carbon matrix.

The high-resolution spectrum of the Ni 2p region showed the formation of Ni 2p_{3/2} at 854.78 eV and

Ni 2p_{1/2} at 872.28 eV exhibiting two general shake-up satellites (Fig. 5). Additionally, a less intense peak arose at 852.58 eV that corresponded to the Ni⁰ region. Formation of the Ni⁰ state supports the XRD results that revealed the recrystallization of pure Ni NPs on the surface of the carbon nanofibers.

3.2 Analysis of kinetic behaviour towards lithium polysulfides

The results of the kinetics studies of LiPS conversion during RedOx reactions are presented by the CV profiles of the symmetrical and Li-S cells with

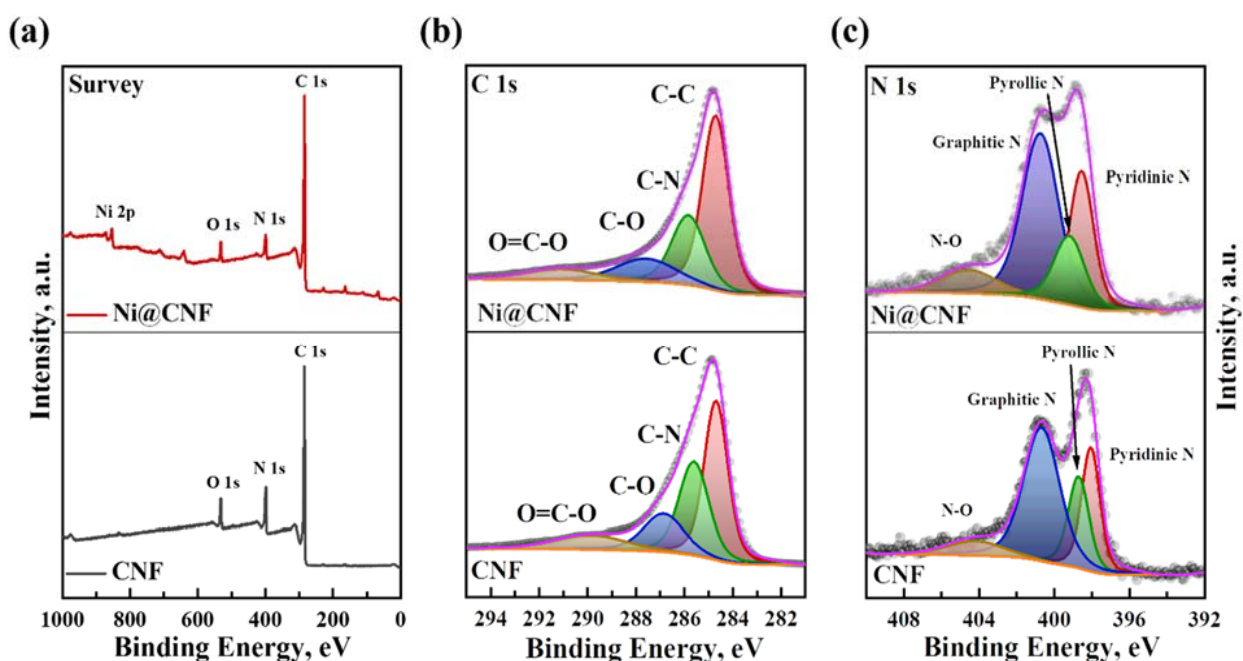


Fig. 4. High-resolution XPS spectra: (a) – Elemental Survey; (b) – C 1s spectra; (c) – N 1s spectra.

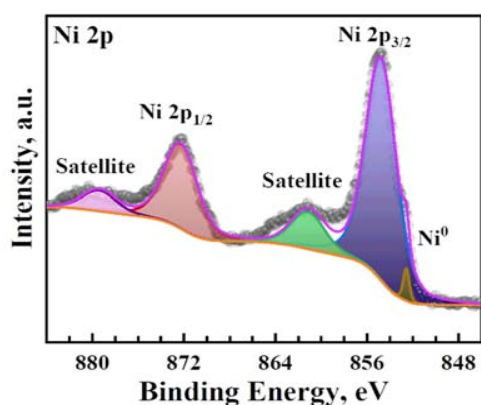


Fig. 5. High-resolution XPS spectra: Ni 2p spectra region.

conventional cathode and interlayer membranes in Fig. 6. Both symmetric cells demonstrated excellent cycling reversibility over five cycles. The cell with Ni@CNF (Fig. 6a) in contrast to the one with CNF (Fig. 6b) generated four reduction/oxidation peaks, which provided crucial information regarding the electrochemical reactions with LiPS on the electrode materials. These findings corresponded to Peak A (-0.028 V) that indicated the reduction of initial S_8 to Li_2S_6 [31]; Peak B (-0.465 V) related

to the reduction of Li_2S_6 on the working electrode and oxidation on the counter electrode [32]; Peak C (0.089 V) which was generated as a result of Li_2S_6 recovering by the oxidation of Li_2S_2/Li_2S on the working electrode [33]; Peak D (0.467 V) pointing to the Li_2S_6 oxidation on the working electrode with subsequent generation of elemental S_8 [33]. Besides the oxidation/reduction peaks appearing, the Ni@CNF symmetric cell demonstrated a higher current response meaning potentially greater specific capacity generation owing to the polar and catalytic nature of Ni NPs. In terms of the Li-S cells with the cathodes and interlayers, the introduction of carbon nanofiber mats showed great reversibility over five cycles. Nevertheless, the CV profiles of Ni@CNF demonstrated lower polarization and potentials shifting between anodic and cathodic peaks current than CNF pointing to the improved kinetics caused by the presence of Ni NPs. Furthermore, a sharper difference in the reduction peaks depth indicated prompter conversion of sulfur species from initial S_8 to short-chained Li_2S_2/Li_2S at 2.309 V, the final step of the discharge process, bypassing the formation of the long-chained $Li_2S_4/Li_2S_6/Li_2S_8$ at 1.989 V. The oxidation process, in turn, demonstrated a similar

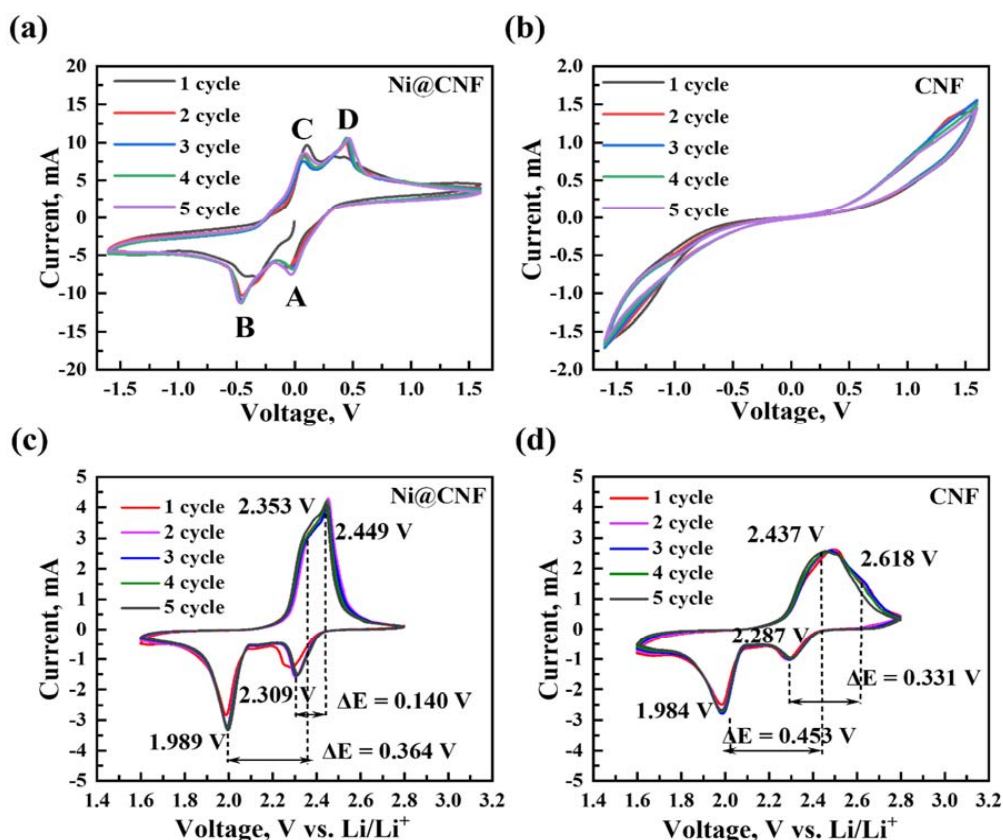


Fig. 6. Cyclic voltammetry test profiles. Symmetric cells test analysis: (a) – Ni@CNF; (b) – CNF; CV profiles of Li-S cells at 0.1 mV s^{-1} scan speed: (c) – Ni@CNF; (d) – CNF.

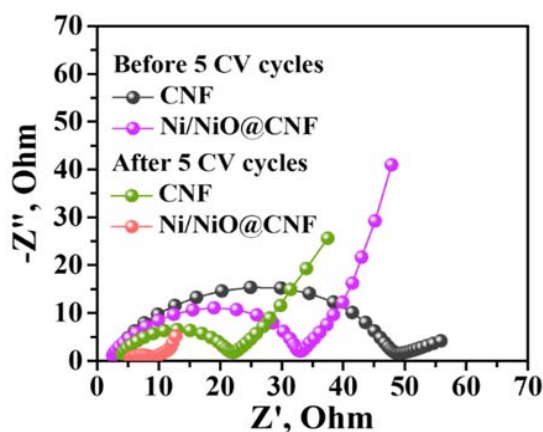


Fig. 7. Potential electrochemical impedance spectroscopy analysis of Li-S cells with Ni@CNF and CNF interlayer membranes.

pattern of two arisen distinguishable peaks at 2.353 V and 2.449 V, among which the latter presented the highest intensity and predominant conversion of $\text{Li}_2\text{S}_2/\text{Li}_2\text{S}$ more into S_8 than accentuating at $\text{Li}_2\text{S}_4/\text{Li}_2\text{S}_6/\text{Li}_2\text{S}_8$.

3.3 Potentiostatic electrochemical impedance spectroscopy analysis

The charge transfer resistance (RCT) during the electrochemical reaction was estimated by potentiostatic electrochemical impedance spectroscopy (PEIS) analysis before and after five CV cycles from the semicircles formed in the medium frequent region and straight lines in the low-frequency area (Fig. 7). According to the findings, the Li-S cell with Ni@CNF retrieved the lowest RCT of 35 Ω before CV and 12 Ω after CV cycling in contrast to the CNF's 69 Ω and 18 Ω , respectively. The decline in RCT value was caused by the presence of carbon nanofiber threads with long electron transfer paths alongside the Ni NPs implementation to the structure providing better electron transfer pathways. Likewise, the lower the value of the charge transfer resistance, the better the electron transfer during the RedOx reactions leading to more stabilized cycles of the electrochemical performance.

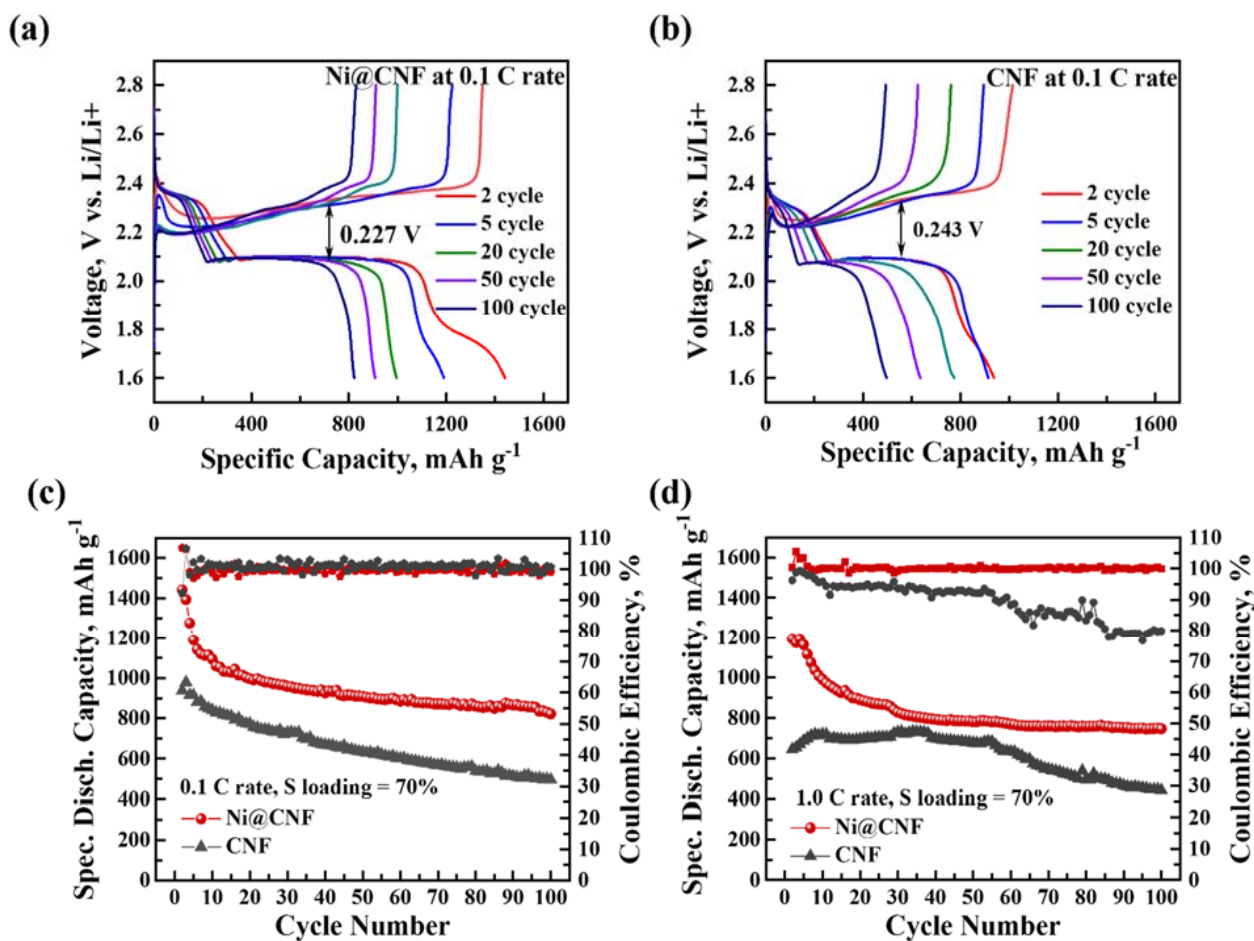


Fig. 8. Galvanostatic charge-discharge cyclability results: (a) – 0.1 C rate cyclability; (b) – 1.0 C rate cyclability; Voltage profiles of: (c) – Ni@CNF; (d) – CNF.

3.4 Electrochemical performance analysis of Li-S cells with CNF and Ni@CNF

The cycling stability effect of the samples was investigated thoroughly via galvanostatic charge-discharge tests at 0.1 and 1.0 C current densities/rates. The potential profiles of Ni@CNF (Fig. 8a) recorded at 0.1 C rate showed a shorter “distance”/lower polarization between the reduction and oxidation peaks position and prolonged plateaus in contrast to CNF (Fig. 8b), pointing to the enhanced kinetics of sulfur species conversion RedOx reactions owing to the presence of Ni NPs. Nevertheless, a noticeable shift during the 2nd discharge cycle of Ni@CNF was related to the decomposition of lithium nitrate at 1.8 V [34]. The charge-discharge cycling profile of a Li-S cell with the Ni@CNF interlayer at 0.1 C rate demonstrated tremendous initial discharge specific capacity of 1441.2 mAh g⁻¹ and demonstrated great cycling stability starting from the 20th cycle with 82.5% capacity retention over 100 cycles. On the other hand, although CNF managed to retrieve a relatively high initial discharge specific capacity of 937.5 mAh g⁻¹, it ended up having worse stability with apparent capacity fade over cycling (Fig. 8c). The same pattern of CNF continued later at a 1.0 C rate with frequent fluctuations in discharge capacity and noticeably rapid capacity fading. Meanwhile, Ni@CNF generated a higher initial discharge capacity of 1194.2 mAh g⁻¹ (Fig. 8d) and presented enhanced stability from the 20th cycle to the 100th cycle along with 83% capacity retention. The significant difference between Ni@CNF and CNF in cycling stability at higher current density demonstrated the beneficial impact of Ni NPs on improving and stabilizing the electrochemical performance of Li-S cells.

4. Conclusions

Herein, the implementation of carbon nanofiber interlayer mats into the Li-S cells and their impact on the electrochemical performance was investigated. Recrystallization of nickel nanoparticles did not have any noticeable changes in the structure of the carbon nanofibers, but strengthened the durability and flexibility of the mats. Moreover, the presence of Ni NPs provided better electron pathways during the electrochemical reactions and great initial discharge capacities of 1441.2 mAh g⁻¹ and 1194.2 mAh g⁻¹ and overall coulombic efficiencies of ~83% at 0.1 C and 1.0 C rates, respectively. The improved electrochemical performance was due to the enhanced kinetics of LiPS conversion during RedOx reactions owing to

the polar and catalytic nature of Ni NPs, a crucial factor in the LiPS chemical anchoring. Thus, the implementation of carbon nanofibers with Ni NPs proved to be a promising way to reduce the shuttle effect and improve the overall efficiency of Li-S batteries.

Acknowledgements

This research paper was carried out as a part of the project AP09259764 “Engineering of Multifunctional Materials of Next-Generation Batteries” from the Ministry of Education and Science of Kazakhstan.

References

- [1]. Z.L. Xu, J.K. Kim, K. Kang, *NanoToday* 19 (2018) 84–107. DOI: [10.1016/j.nantod.2018.02.006](https://doi.org/10.1016/j.nantod.2018.02.006)
- [2]. T.O. Ely, D. Kamzabek, D. Chakraborty, M.F. Doherty, *ACS Appl. Energy Mater.* 1 (2018) 1783–1814. DOI: [10.1021/acsaem.7b00153](https://doi.org/10.1021/acsaem.7b00153)
- [3]. B. Moorthy, S. Kwon, J.H. Kim, P. Ragupathy, H.M. Lee, D.K. Kim, *Nanoscale Horizons* 4 (2019) 214–222. DOI: [10.1039/c8nh00172c](https://doi.org/10.1039/c8nh00172c)
- [4]. Y.J. Li, J. M. Fan, M. Sen Zheng, Q.F. Dong, *Energy Environ. Sci.* 9 (2016) 1998–2004. DOI: [10.1039/c6ee00104a](https://doi.org/10.1039/c6ee00104a)
- [5]. D. Liu, C. Zhang, G. Zhou, W. Lv, et al., *Adv. Sci.* 5 (2018). DOI: [10.1002/adv.201700270](https://doi.org/10.1002/adv.201700270)
- [6]. H. Qiu, T. Wang, W. Lv, Q. Liu, J. Huang, *J. Colloid Interface Sci.* 630 (2023) 106–114. DOI: [10.1016/j.jcis.2022.10.006](https://doi.org/10.1016/j.jcis.2022.10.006)
- [7]. J.W. Guo, M.S. Wu, *Electrochim. Acta* 327 (2019) 135028. DOI: [10.1016/j.electacta.2019.135028](https://doi.org/10.1016/j.electacta.2019.135028)
- [8]. N. Li, Y. Xie, S. Peng, X. Xiong, K. Han, *J. Energy Chem.* 42 (2020) 116–125. DOI: [10.1016/j.jchem.2019.06.014](https://doi.org/10.1016/j.jchem.2019.06.014)
- [9]. N. Baikalov, I. Rakhimbek, A. Konarov, A. Mentbayeva, Y. Zhang, Z. Bakenov, *RSC Adv.* 13 (2023) 9428–9440. DOI: [10.1039/d3ra00891f](https://doi.org/10.1039/d3ra00891f)
- [10]. J. Liu, C. Hu, H. Li, N. Baikalov, Z. Bakenov, Y. Zhao, *J. Alloys Compd.* 871 (2021) 159576. DOI: [10.1016/j.jallcom.2021.159576](https://doi.org/10.1016/j.jallcom.2021.159576)
- [11]. M. Wang, X. Xia, Y. Zhong, J. Wu, et al., *Chem. – A Eur. J.* 25 (2019) 3710–3725. DOI: [10.1002/chem.201803153](https://doi.org/10.1002/chem.201803153)
- [12]. Z. He, T. Wan, Y. Luo, G. Liu, et al., *Chem. Eng. J.*, 448 (2022) 137656. DOI: [10.1016/j.cej.2022.137656](https://doi.org/10.1016/j.cej.2022.137656)
- [13]. L. Wang, Z.Y. Wang, J.F. Wu, G.R. Li, et al., *Nano Energy* 77 (2020) 105173. DOI: [10.1016/j.nanoen.2020.105173](https://doi.org/10.1016/j.nanoen.2020.105173)
- [14]. S. Yao, H. Tang, M. Liu, L. Chen, *J. Alloys Compd.* 788 (2019) 639–648. DOI: [10.1016/j.jallcom.2019.02.236](https://doi.org/10.1016/j.jallcom.2019.02.236)
- [15]. Zhang Ling, Bi Jiaying, Zhao Zhikun, Wang

- Yuxin, Daobin Mu, Borong Wu, *Electrochim. Acta* 370 (2021) 137759. DOI: [10.1016/j.electacta.2021.137759](https://doi.org/10.1016/j.electacta.2021.137759)
- [16]. C. Qi, Z. Li, C. Sun, C. Chen, J. Jin, Z. Wen, *ACS Appl. Mater. Interfaces* 12 (2020) 49626–49635. DOI: [10.1021/acsami.0c14260](https://doi.org/10.1021/acsami.0c14260)
- [17]. Y. Liu, G. Feng, X. Guo, Z. Wu, et al., *J. Alloys Compd.* 748 (2018) 100–110. DOI: [10.1016/j.jallcom.2018.03.110](https://doi.org/10.1016/j.jallcom.2018.03.110)
- [18]. H.B. Kim, D.T. Nga, R. Verma, Y.N. Singhababu, et al., *Ceram. Int.* 47 (2021) 21476–21489. DOI: [10.1016/j.ceramint.2021.04.159](https://doi.org/10.1016/j.ceramint.2021.04.159)
- [19]. M. Chen, X. Zhao, Y. Li, P. Zeng, et al., *Chem. Eng. J.* 385 (2020). DOI: [10.1016/j.cej.2019.123905](https://doi.org/10.1016/j.cej.2019.123905)
- [20]. L. Zhang, D. Liu, Z. Muhammad, F. Wan, et al., *Adv. Mater.* 31 (2019) 1903955. DOI: [10.1002/adma.201903955](https://doi.org/10.1002/adma.201903955)
- [21]. Y. Huang, D. Lv, Z. Zhang, Y. Ding, et al., *Chem. Eng. J.* 387 (2019) 124122. DOI: [10.1016/j.cej.2020.124122](https://doi.org/10.1016/j.cej.2020.124122)
- [22]. Y. Guo, J. Li, R. Pitcheri, J. Zhu, P. Wen, Y. Qiu, *Chem. Eng. J.* 355 (2018) 390–398. DOI: [10.1016/j.cej.2018.08.143](https://doi.org/10.1016/j.cej.2018.08.143)
- [23]. X. Zhang, W. Yuan, Y. Yang, S. Yang, *J. Colloid Interface Sci.* 583 (2021) 157–165. DOI: [10.1016/j.jcis.2020.09.020](https://doi.org/10.1016/j.jcis.2020.09.020)
- [24]. Y. Fu, J. Hu, Q. Wang, D. Lin, K. Li, L. Zhou, *Carbon* 150 (2019) 76–84. DOI: [10.1016/j.carbon.2019.05.008](https://doi.org/10.1016/j.carbon.2019.05.008)
- [25]. D. An, L. Shen, D. Lei, L. Wang, H. Ye, *J. Energy Chem.* 31 (2019) 19–26. DOI: [10.1016/j.jechem.2018.05.002](https://doi.org/10.1016/j.jechem.2018.05.002)
- [26]. J. Zhu, Y. Liu, L. Zhong, J. Wang, H. Chen, *J. Electroanal. Chem.* 881 (2021) 114950. DOI: [10.1016/j.jelechem.2020.114950](https://doi.org/10.1016/j.jelechem.2020.114950)
- [27]. Z. Sun, Y. Guo, B. Li, T. Tan, Y. Zhao, *Solid State Sci.* 95 (2019) 105924. DOI: [10.1016/j.solidstatesciences.2019.06.013](https://doi.org/10.1016/j.solidstatesciences.2019.06.013)
- [28]. L. Jiang, H. Yi, C. Zhongling, P. Peng, et al., *Electrochim. Acta* 375 (2021). DOI: [10.1016/j.electacta.2021.137993](https://doi.org/10.1016/j.electacta.2021.137993)
- [29]. S. Das and M. Saha, *J. Pharm. Anal.* 4 (2014) 351–359. DOI: [10.1016/j.jpha.2014.03.004](https://doi.org/10.1016/j.jpha.2014.03.004)
- [30]. L. Li, G. Xu, X. Liu, S. Huang, X. Wei, L. Yang, *J. Power Sources* 506 (2021) 230177. DOI: [10.1016/j.jpowsour.2021.230177](https://doi.org/10.1016/j.jpowsour.2021.230177)
- [31]. F. Ma, Z. Chen, K. Srinivas, D. Liu, et al., *Chem. Eng. J.* 459 (2023) 141526. DOI: [10.1016/j.cej.2023.141526](https://doi.org/10.1016/j.cej.2023.141526)
- [32]. L. Gao, T. Sheng, H. Ran, T.X. Liu, *Appl. Surf. Sci.* 597 (2022) 153687. DOI: [10.1016/j.apsusc.2022.153687](https://doi.org/10.1016/j.apsusc.2022.153687)
- [33]. A. Belgibayeva, I. Taniguchi, *J. Power Sources* 484 (2021) 229308. DOI: [10.1016/j.jpowsour.2020.229308](https://doi.org/10.1016/j.jpowsour.2020.229308)
- [34]. S.S. Zhang, *J. Power Sources* 322 (2016) 99–105. DOI: [10.1016/j.jpowsour.2016.05.009](https://doi.org/10.1016/j.jpowsour.2016.05.009)